



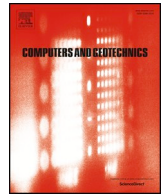
Numerical analyses of an experimental excavation supported by panels of lime-cement columns

Downloaded from: <https://research.chalmers.se>, 2024-04-25 21:14 UTC

Citation for the original published paper (version of record):

Ignat, R., Baker, S., Karstunen, M. et al (2020). Numerical analyses of an experimental excavation supported by panels of lime-cement columns. *Computers and Geotechnics*, 118.
<http://dx.doi.org/10.1016/j.compgeo.2019.103296>

N.B. When citing this work, cite the original published paper.



Research Paper

Numerical analyses of an experimental excavation supported by panels of lime-cement columns

Razvan Ignat^{a,*}, Sadek Baker^b, Minna Karstunen^c, Sven Liedberg^b, Stefan Larsson^d^a Department of Civil and Architectural Engineering, Royal Institute of Technology, SE 100 44 Stockholm, Sweden^b Skanska Sweden AB, Stockholm, Sweden^c Department of Architecture and Civil Engineering, Chalmers University of Technology, Sweden^d Department of Civil and Architectural Engineering, Royal Institute of Technology, Sweden

ARTICLE INFO

Keywords:

Deep mixing columns
Finite element analyses
Strength anisotropy
Deep excavation

ABSTRACT

The influence of ground improvement with panels of overlapping lime-cement columns on the behavior of a braced excavation loaded to failure has been investigated using 3D numerical analyses and the results are compared with an experimental full-scale failure test. The analyses reveal that stress-induced strength anisotropy of lime-cement improved clay needs to be considered when the stress path for the actual field conditions differs from that in conventional laboratory testing. In addition to strength parameters, the modulus of deformation that is consistent with the actual encountered stress path is also needed for reasonable predictions.

1. Introduction

Excavations in soft clay deposits in urban areas are one of the most challenging problems for geotechnical design engineers, due to the large ground displacements resulting in a risk of damaging adjacent structures. To reduce excavation induced displacements, and to improve the safety against basal heave failure, different ground improvement techniques have been employed. These include jet grouting and deep mixing, thus creating soil/cement columns in the passive zone [1–6]. Several FE-studies regarding the effect of soil improvement by deep mixing in reducing the excavation induced wall displacements and the structural forces in the retaining structures have been presented [7–13]. In the majority of these studies, the concept of composite material has been adopted to represent the material properties of the improved soil. An isotropic strength for the columns, normally evaluated from unconfined compression tests, UC, is commonly used in practice. However, several researchers [14–17] have highlighted that the isotropic strength may not represent the actual performance of deep mixing columns in the passive zone. Thus, they have introduced strength reduction factors to the material composite strength to account for the stress-induced anisotropy. Although promising, these studies are generally based on hypothetical excavations. The pre- and post-failure behavior of a full-scale column-type ground improvement supported excavation has not been documented in field conditions.

To investigate the field behavior and the efficiency of ground improvement with lime-cement columns, LCC, in the passive zone of an

excavation, two full-scale tests were performed during 2014 in Enköping, located in the Eastern part of Sweden. Both tests were comprehensively instrumented. The test set-up, test execution and the results from the field tests have been presented in a previous publication [18]. Basically, excavations with braced sheet pile walls supported by panels of overlapping LCC were first excavated, and then brought to failure by applying a stepwise increasing load behind the sheet pile wall. The LCCs installed in the passive zone were thereby subjected to first unloading, and then lateral loading during the excavation and loading to failure. The set-up was designed to isolate the failure due to excessive horizontal movements as the main mode of failure. In order to generalize the results, and have confidence in future predictions, the results need to be analyzed with the help of numerical modelling.

This paper presents numerical analyses of the failure tests of full-scale excavations supported by panels of LCC. The Hardening Soil model (HS), [19], implemented in Plaxis was used to describe the stress-strain behavior of LCC. The dependency of the undrained shear strength, $s_{u,col}$, on the stress path to failure was also considered. This was done by assessing the strength based on results from isotropically consolidated undrained triaxial extension tests, CIUE, conducted under stress paths to failure similar to the theoretical stress paths in the experimental LCC panels. The post-peak behavior of the strength and the stiffness anisotropy of the soft clay was considered by deriving parameters from anisotropically consolidated undrained triaxial compression and extension tests, CK_0UC and CK_0UE , and constant rate of strain oedometer tests (CRS). The parameters were then used in the

* Corresponding author.

E-mail addresses: razvani@kth.se, razvan.ignat@kerberosgeo.se (R. Ignat).

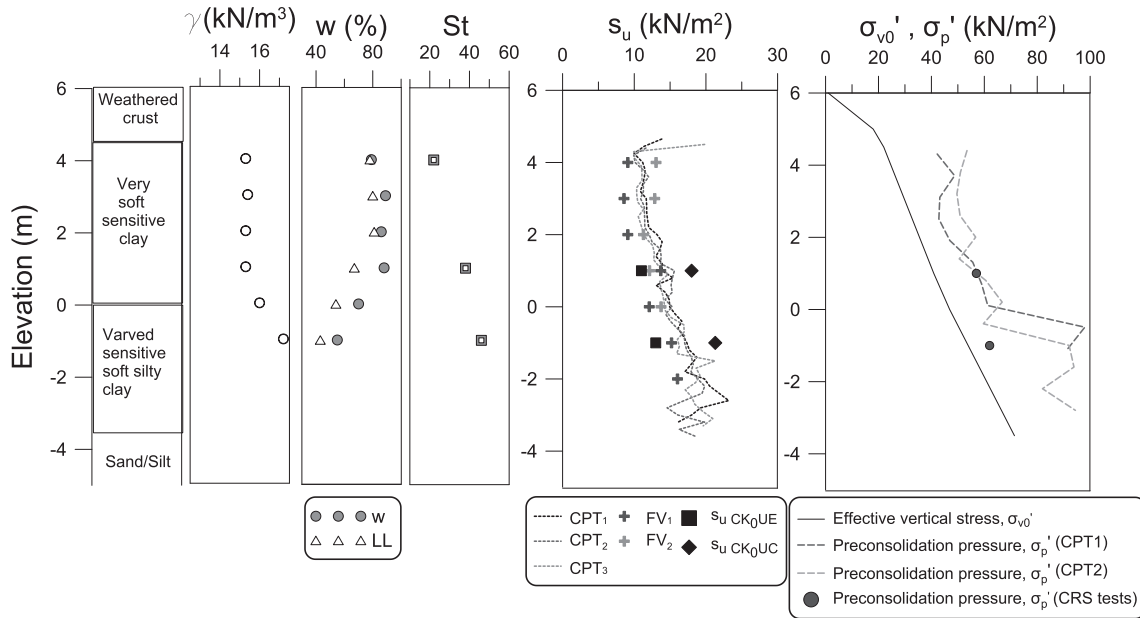


Fig. 1. Basic material properties of the soft clay at the test site.

constitutive model S-Clay1S developed by Koskinen et al. [20] and Karstunen et al. [21], implemented in Plaxis 3D by Sivasithamparam [22].

2. Geotechnical conditions and test description

The general stratigraphy and conditions at the test site are presented in Fig. 1 and are described in detail by Ignat et al., 2016 [18]. Below the ground surface there is a 1.0–1.5 m thick layer of weathered clay crust, on top of a soft post-glacial clay layer with a thickness of 7–9 m. Under the clay there is a 3–7 m thick deposit of silt and sand, followed by a thin layer of stiff till closest to the bedrock. Down to a depth of approximately 5–5.5 m, lenses of sulfide bearing clay occur and the clay has a high water content, w , of 80 to 90% and a liquid limit, w_L , of 67–81%. The clay layer below this depth was classified as banded silty clay with a significantly lower w and w_L , 55–70% and 40–53%, respectively, and with a unit weight that increases with depth. The vertical pre-consolidation pressure, σ_p' , evaluated from constant rate of strain oedometer tests, CRS tests, suggests that the clay is lightly over-consolidated with an OCR of about 1.5 and 1.2 at 5 and 7 m depth, respectively. The undrained shear strength of the clay, s_u , determined from site field vane shear tests and CPT tests was 9–11 kPa from the top of the soft clay layer to a level of about 4 m below the ground surface, and showed an average strength increase of about 1.1 kPa/m below this level. The sensitivity of the clay, S_t , increased with depth from about 20 at 2 m depth to 50 at 7 m depth, and was classified as highly sensitive below 5 m depth, $S_t > 30$.

The dependency of s_u on the stress path followed during undrained shearing (stress-induced anisotropy), a feature typical of soft Scandinavian clays [21,23–28], was investigated by means of CK₀UC and CK₀UE tests conducted on undisturbed clay samples collected from depths of 5 and 7 m, respectively [29]. The clay at the test site exhibits not only anisotropy, but also significant reduction of s_u with further straining after reaching a peak value. This strain softening, evidenced in the CK₀UC tests, is a characteristic behavior for sensitive soft clays [30,31].

The results of s_u normalized by the vertical consolidation stress, σ_v' , as a function of OCR are presented in Fig. 2, together with established empirical relationships for the anisotropy of s_u for Scandinavian clays [26,32] derived based on the SHANSEP methodology, presented for artificially overconsolidated clays [33,34]. The evaluated anisotropy

ratio, s_u^E/s_u^C , varied between 0.66 and 0.75, which is in line with previous results for Scandinavian clays [24] and other soft clays [35–38].

2.1. Field test set-up

Two separate full-scale tests were performed to study braced sheet pile walls, SPW, supported by panels of overlapping LCC. Except for the center distance between the LCC panels, s_{panel} , chosen to be 3.0 m in Test A and 1.5 m in Test B, all other geometric and material parameters of the retaining structure were identical. In each test two SPWs with a crest length of 20 m were installed parallel to each other so that the width of each excavation pit was equal to 12 m. The SPWs were installed to a depth of 7 m on the loaded side and 7.5 m below the ground surface on the opposing side. The wall was not driven to the sand layer underneath, to simulate the use of LCC panels against excessive lateral movements in excavations on soft clays. Overlapping LCC with a diameter of 0.6 m and center distance of 0.5 m between each column were installed all the way to the frictional soil layer below the soft clay in a panel wall configuration between the two SPWs. The geometrical layout of the tests including the LCC panels, the SPWs and bracing system and excavation level are presented in Fig. 3. The location of the instrumentation used in these tests (including earth pressure cells, inclinometers, pore pressure transducers, strain gauges mounted on the strut beams) have also been included in Fig. 3 to explain the field test results presented. This way the failure mechanism due to excessive lateral movements can be isolated from the combination of that and the failure due to bottom-uplift.

The LCCs were manufactured by the Scandinavian dry deep mixing method, (CEN 2005). The amount of binder was chosen to be 120 kg/m³, 50% quicklime and 50% Portland cement. The SPWs in both tests were braced with steel beams installed at a center distance of 3.0 m. Both tests were instrumented with inclinometers, earth pressure cells and pore pressure transducers on the active and the passive side of the SPWs, both in the column panels and in the clay. In addition, strain gauges were installed on the steel structures. A similar construction sequence, as described in Table 1, was adopted in both tests. To load the structure to failure two containers placed on steel frames above a stiff Load Distribution Platform, LDP, on the active side were filled with soil. The load in the containers was measured by 4 load cells centric located under each container frame and the total applied distributed load behind the SPW, including the weight of the LDP, is presented as sq_{load} .

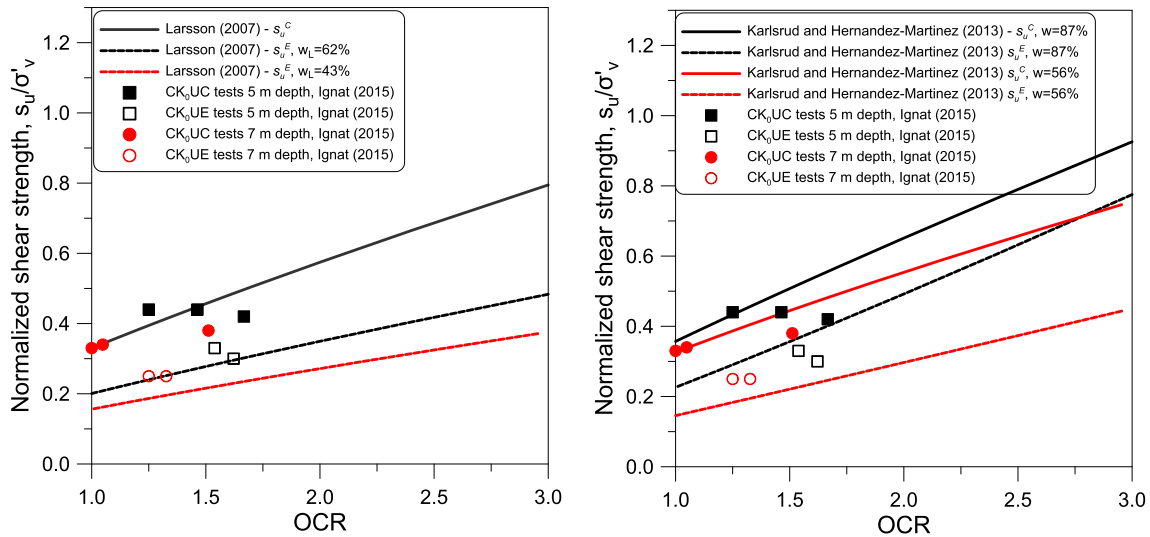


Fig. 2. Measured normalized peak shear strength of soft clay versus OCR and empirical relationship for Scandinavian clays.

In Test A, $s_{panel} = 3.0$ m, a failure emerged about 10 h after the loading process started. In Test B, $s_{panel} = 1.5$ m, a failure emerged about 50 h after the loading process started. Following an initial loading process with duration of approximately 30 h in Test B, an additional excavation of 0.5 m was conducted after partial unloading of the containers. The unloading was necessary to perform a safe additional excavation before the containers were loaded again and the structure was brought to failure. A detailed description of the construction sequence of Test B is presented in [18]. The structure was thereafter monitored for a period of 14 h before the load was again increased in one step and brought to failure.

2.2. Field test results

The results of the field tests are described in full detail in [18], and are only briefly presented here. In both tests the developed failure mechanisms were identified as a stability failure of the SPWs, resulting in large displacements at the bottom of the excavation and at ground level on the active side of the SPW. The horizontal displacements, u_h , measured in the clay behind the SPW and in the clay and LCC panels in front of the SPW (at the same distance from the SPW and depth below excavation), before and during failure of Test A and Test B respectively, are presented in Fig. 4. To clarify the propagation of the failure, the horizontal stress change in the LCC panels, $\Delta\sigma_{hcol}$, and the magnitude of the applied load behind the SPW, q , have been included in the figure. A peak load, defined as the maximum applied load, q_{peak} , of 40.6 kPa was measured after the last load step was applied in Test A, about 7.5 h after the start of the loading process, illustrated in Fig. 4. A failure load, q_{fail} , characterized by a sudden large drop of $\Delta\sigma_{hcol}$ and an increase of u_h , equal to 39.0 kPa, was observed 2.5 h later, followed by a further load drop post-failure, due to the tilting of the containers. In Test B, after unloading to 40 kPa (70% of the applied load) an additional excavation of 0.5 m was conducted and monitored for 14 h, before the load was again increased in one step to q_{peak} of 56 kPa. The last load step was applied at a faster rate than the previous load steps, and the load immediately started to gradually decrease until failure, $q_{fail} = 50.5$ kPa, followed by a sudden load drop to 40 kPa post-failure.

Although the same overall failure mechanism was obtained in both tests, significant differences between the pre- and post-failure behavior in the two tests were observed. In particular, the failure in Test A was initiated in the clay between the column-panels due to the large LCC panel center distance, whilst the failure in Test B was initiated simultaneously in the LCC panels and the clay between the panels.

Failure in Test A was sudden, with very small deformations observed pre-failure, and a total collapse of the structure with very large post-failure displacements.

Observations of horizontal stress change, $\Delta\sigma_{hcol}$ and $\Delta\sigma_{hclay}$ (only $\Delta\sigma_{hcol}$ presented in Fig. 4), and horizontal displacements, u_h , indicated that a local failure was initiated in the clay between the column panels, followed by failure of the LCC panels close to the SPW. After the last load step was applied, the columns started to yield ($\Delta\sigma_{hcol}$ started to decrease) initiating load transfer to the clay between the panels ($\Delta\sigma_{hclay}$ started to increase). Prior to failure u_h in the clay, in both the active and the passive zone, increased at a faster rate than in the columns, and a sudden local failure occurred in the clay between the LCC panels in front of the Load Distribution Platform (LDP). This was immediately followed by failure of the adjacent LCC panels close to the SPW, displayed as a large drop in $\Delta\sigma_{hcol}$ and sharp increase in u_h , resulting in a total collapse of the structure.

In Test B the columns started to yield during the final loading stage, and the decrease in $\Delta\sigma_{hcol}$ occurred at a significantly faster rate than in Test A, followed by an equal increase in u_h in both column panels and the clay between the panels. A large drop in $\Delta\sigma_{hcol}$ was measured at the time of failure. However, contrary to Test A, no total collapse of the structure occurred. At failure in Test B, very similar u_h was registered in both the column panels and the clay between the panels at equal distance from the SPW, indicating a simultaneous failure of the LCC panels and the clay between the panels in front of the LDP.

2.3. Triaxial extension behavior of lime-cement admixed clay

The strength and the stiffness properties of improved clays are normally assessed based on results from UC tests. However, the loading conditions in the field tests, involving unloading and lateral loading, deviate significantly from those imposed in a conventional UC test. Clay collected from the test site, from a depth of 5.5–6.5 m, was mixed in the laboratory with a binder content of 120 kg/m³, 50% quicklime, QL 0–0.1 KÖ, and 50% Portland cement, CEM II/A-LL 42.5 R, similar to the dry binder content used in the full-scale field tests, see [39] for details. After mixing, the samples were sealed with rubber lids before being stored for 28 days in a climate room at 7 °C without curing stress. Isotropically consolidated undrained triaxial extension tests, CIUE, on the laboratory mixed lime-cement improved clay were conducted at different consolidation stresses, σ'_c , to investigate the material stress-strain behavior sheared under different triaxial stress paths, [39]. Isotropically consolidated undrained compression triaxial tests, CIUC,

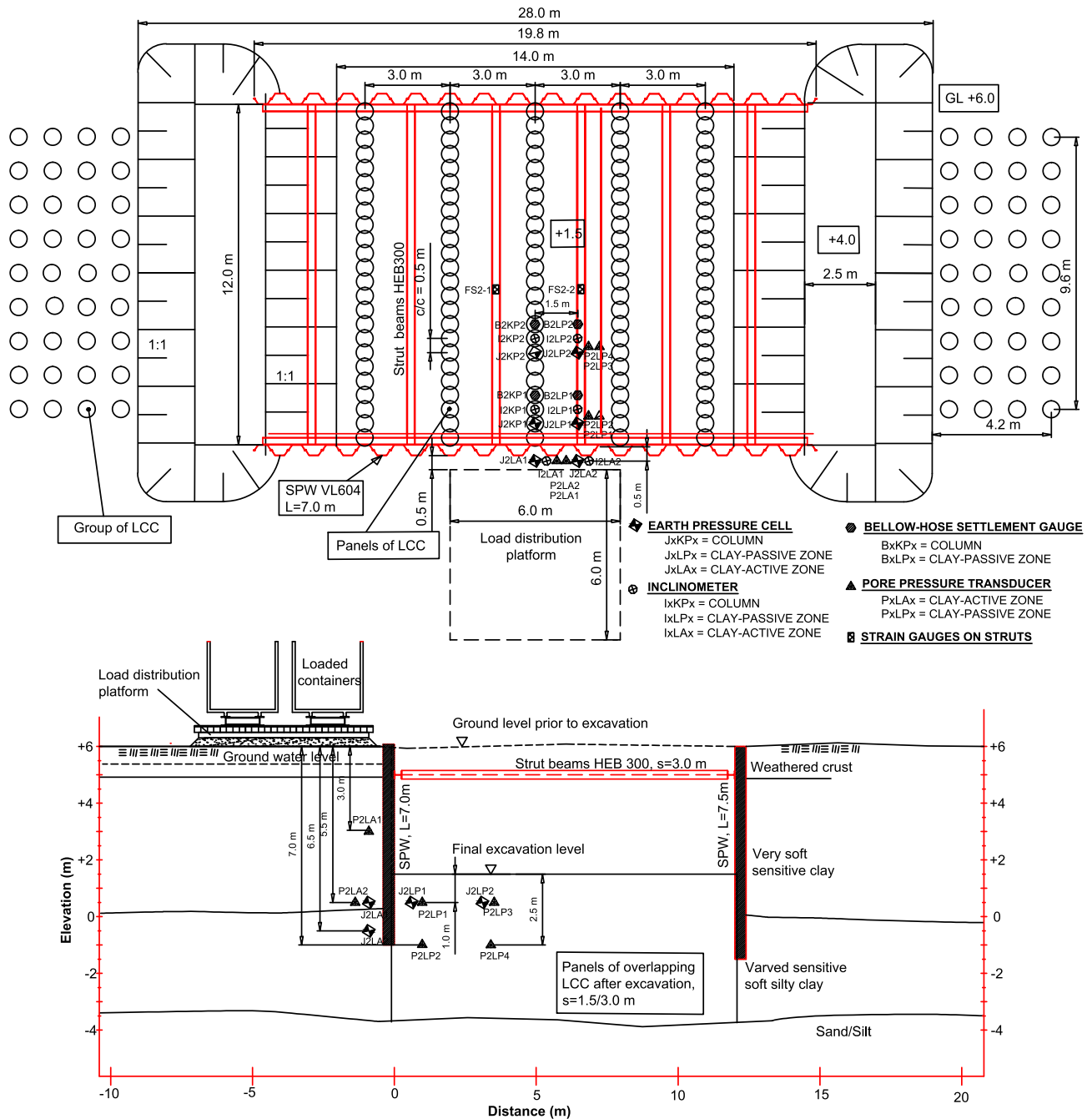


Fig. 3. Geometrical layout and instrumentation of the experimental tests.

were also conducted for comparison. Three different stress paths were investigated: triaxial extension, CIUE-L (increase in radial stress under constant axial stress), triaxial tension, CIUE-U (decrease in axial stress under constant radial stress), and a stress path where a decrease in axial stress and increase in radial stress were applied simultaneously, CIUE-UL, analogous to stress paths anticipated in the field experiments. Increase in radial stress and decrease in axial stress resembles the stress change in the LCC close to the SPW during excavation. Results are presented in Fig. 5, in terms of the measured peak deviator stress, q_f , normalized by applied σ'_c as a function of OCR, as well as the relationship between q_f and the secant modulus, E_{50} . Test results strongly indicate that q_f is stress path -dependent and the material exhibits

significant stress-induced anisotropy at low values of σ'_c . However, the differences in q_f between different applied stress paths decreases with increasing σ'_c .

Based on CIUC and CIUE-L tests q_f normalized to σ'_c was related to OCR according to the SHANSEP methodology, as was also shown by Åhnberg [40] and Kasama et al. [41] for improved soil. For unloading stress paths, CIUE-U and CIUE-UL, q_f was less dependent on OCR, resulting in a different relationship between q_f , OCR, and σ'_c , illustrated in Fig. 5.

A much lower strain at failure was observed in the extension tests compared to the compression tests (both CIUC and UC), resulting in significantly higher mobilized E_{50} . Independently of applied stress path,

Table 1
Construction sequence of the experimental tests.

Stage	Feature	Elapsed time Test A (days)	Elapsed time Test B (days)
1	Installation of LCC panels by the dry DMM	1	1
2	Installation of the SPW	1	1
3	Installation of group of LCC	2	2
4	Excavation to level +4.0	22–24	24–28
5	Installation of the strut system	25–29	31–35
6	Excavation to level +2.0	30–31	–
7	Excavation to level +1.5	35	43*
8	Construction of stiff load distribution platform, LDP, 6×6 m, positioned 0.5 m from the SPW	35	44
9	Stepwise increased load - applied by filling two containers ($L \times B \times H = 6.3 \times 2.6 \times 2.5$ m) with soil material, start of loading at $t = 0$	36 (failure at $t = 9:55$ h after start of loading)	49–50
10	Unloading and additional excavation to level +1.0	–	50
11	Stepwise increased load	–	51 (failure at $t = 49:50$ h after start of loading)

* Stage 6 and 7 were conducted simultaneously in Test B.

the tests indicated a linear relationship between E_{50} and q_f , where E_{50} in extension tests varied between 440 and 680 q_f , with the lowest ratio from CIUE-U tests and the highest from CIUE-L tests.

3. Finite element analyses of field tests

3.1. Finite element model and boundary conditions

The finite element program Plaxis 3D version 2017.0 was used to simulate the full-scale field tests. For the soil, 10-noded tetrahedral volume elements were used and the volume pile technique was used to model the overlapping LCCs forming the panels between the SPWs. The SPWs were modeled with six-noded triangular plate elements, while beam elements were used to model the strut system. The boundary conditions in the FE model were chosen such that the bottom boundary was fully fixed. The vertical model boundaries parallel to the yz-plane were fixed in the x direction and free in the y and z directions, while vertical model boundaries parallel to the xz plane were fixed in the y direction and free in the x and z directions. Due to symmetry conditions, one half of the geometry of each test was modeled and in order to avoid boundary effects the length and width of the model were chosen to be 56 m and 30 m, respectively (see Fig. 6).

To reduce the number of elements, the thickness of the frictional soil

below the soft clay included in the model was 2 m, resulting in 247 000 elements in the 3D finite element mesh for Test A, presented in Fig. 6, and 306 000 elements for Test B. In order to keep the calculation time within reasonable period, a convergence criterion of 4% was chosen.

A construction sequence similar to the construction sequence of the field tests was chosen, assuming undrained conditions. The initial stresses were generated by the “ K_0 ” procedure adopted in Plaxis as the soil layers were simplified and assumed to be horizontal. In the next two steps the LCC panels and the SPWs were activated. The LCCs were “wished in place”, implying that no volume strain or disturbance of the clay affecting its parameters was taken into consideration. Interface elements on both sides of the sheet pile wall were defined in order to consider the adhesion between the soil and the steel structure. Excavation to final depth was conducted in two steps and the strut system was activated after the first excavation step. The LDP, simulated as a rigid block (linear elastic material) with a thickness of 0.5 m and corresponding unit weight, was activated after the last excavation step. The loading process was simulated by activating a distributed load on top of the LDP, increased in constant steps of 10 kPa until a failure collapse mechanism was obtained. The failure mechanism “soil body collapse” in Plaxis occurred, when the specified load increment for the stage in question was not reached and the applied load was reduced in magnitude in five successive calculation steps whereby the calculation

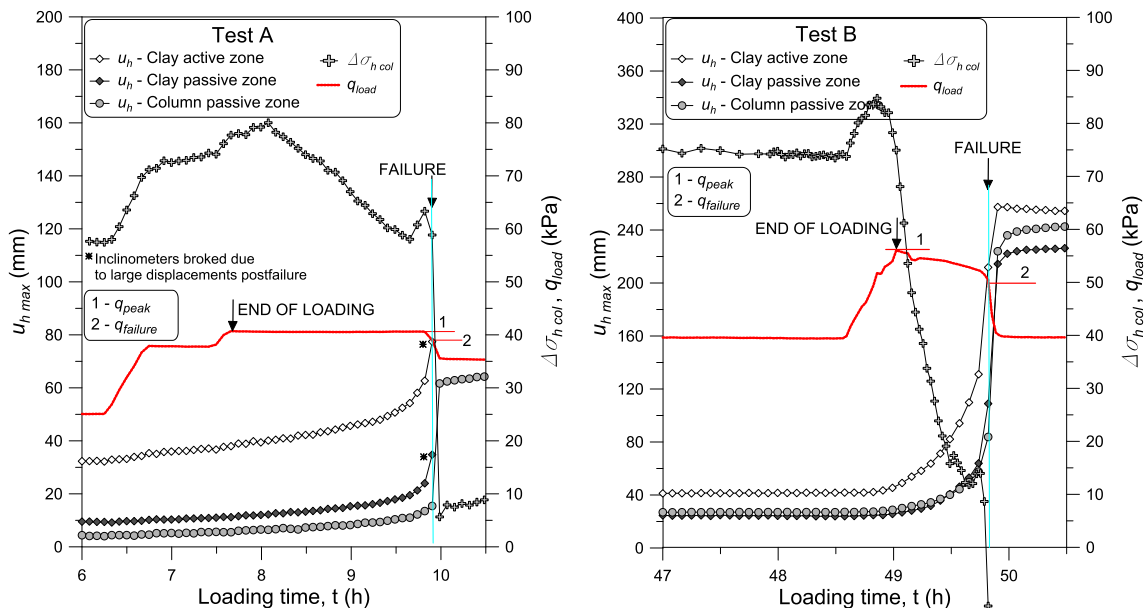


Fig. 4. Experiential horizontal displacements and stress changes in the column panels at failure.

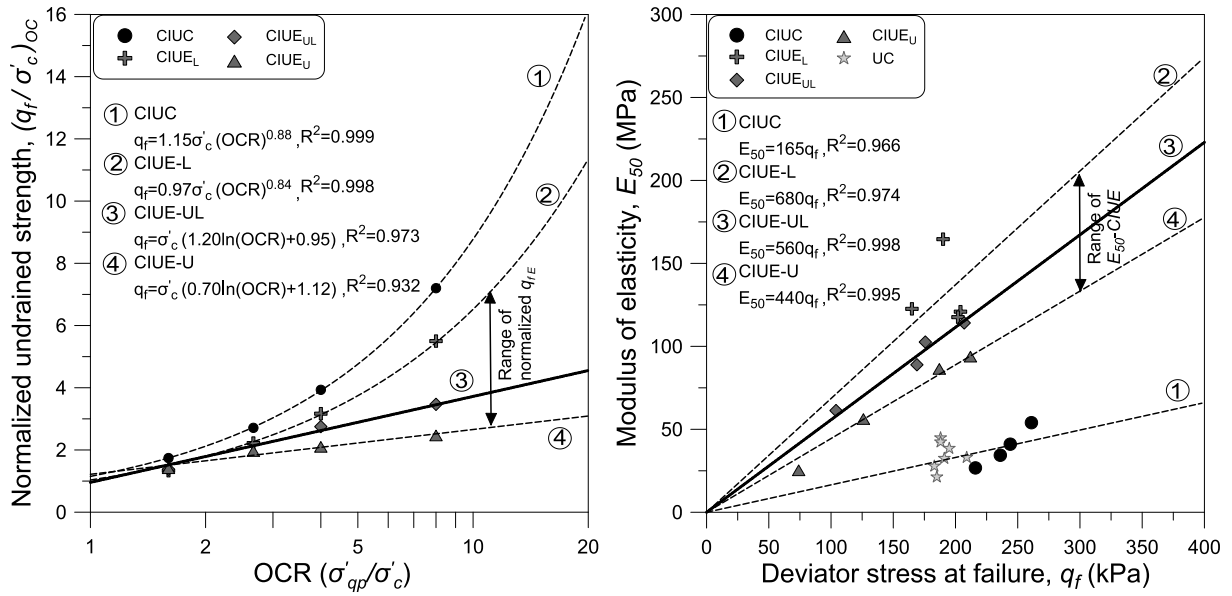


Fig. 5. Strength and stiffness properties of lime-cement improved clay from triaxial laboratory tests.

was terminated. For comparison with the experimental tests, the maximum load that could be applied before reduction was chosen as q_{peak} and the resulting load at “soil body collapse” was chosen as q_{fail} . The construction sequence of Test B followed that of the field test with a partial unloading, and an additional excavation, before the final load step was applied. The time sequence was not taken into consideration in the analyses, as both the excavation and the loading process were conducted over a relatively short period of time and undrained conditions prevailed.

3.2. Constitutive models and model parameters

3.2.1. Soft clay

The model adopted in this study, S-Clay1S, developed by Koskinen et al. [20] and Karstunen et al. [21] originates from critical state models, and is a further development of the S-Clay1 model presented by Wheeler et al. [42]. Similar to S-Clay1 the model adopts an inclined

yield surface to take initial anisotropy into consideration, and a rotational component of hardening to represent the development fabric anisotropy during plastic straining. In addition, the S-Clay1S model also incorporates the influence of bonding and destructuration by introducing an intrinsic yield surface, as presented by Gens and Nova [43], which is necessary when modelling sensitive clays. Both S-Clay1 and its extension S-Clay1S have been successfully validated against experimental laboratory results for several typical Scandinavian soft clays [44–47] and a full description of the model mathematical formulation is presented by Sivasithamparam [22] and is not repeated here.

Model parameters for the FE analyses were obtained by calibrating the CK₀UC and CK₀UE test using the Plaxis “soil test” facility. Evaluated material parameters for S-Clay 1S are presented in Table 2 and Table 3. The over-consolidation was represented by a vertical pre-overburden pressure, POP ($= \sigma_{vp} - \sigma_{v0}$ where σ_{vp} is the vertical pre-consolidation stress and σ_{v0} is the in situ vertical effective stress). The compression

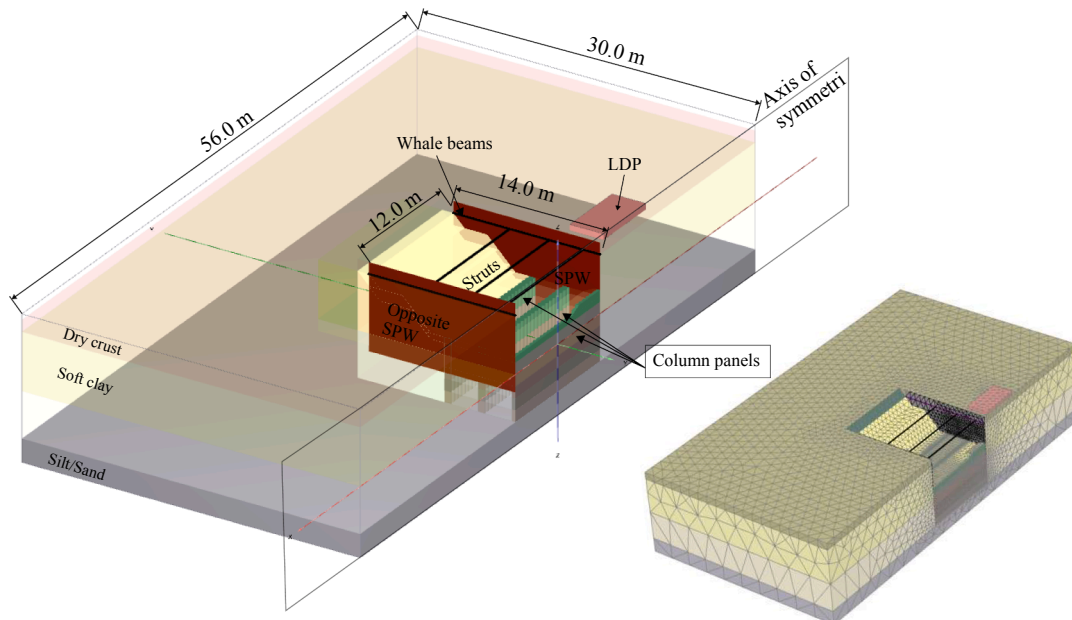


Fig. 6. Model geometry and FE mesh of Test A.

Table 2
Conventional clay parameters.

Layer	Depth	γ	e_0	v'_u	κ	λ	POP	Rinter	
								c'	ϕ'
1	1–6	15.4	2.22	0.15	0.022*	0.550	18	1.0	10.0
2	6–10	17.1	1.57	0.15	0.014*	0.440	12	1.0	10.0

* Chosen as 0.3κ evaluated from computed Plaxis “soil tests”.

Table 3
Clay parameters in S-Clay1S.

Layer	Depth	λ_i	M_c/M_e^*	α_0	μ	β	χ_0	a^{**}	b^{**}
1	1–6	0.165	1.3/0.91	0.50	20	0.87	32	10	0.6*** / 0.2
2	6–10	0.132	1.2/0.86	0.46	20	0.76	50	10	0.6*** / 0.2

* Compression/Extension critical state ratio chosen in the clay on the active/passive side of the SPW.

** For calculation of lower and upper bound values the ratio $\lambda_i/\lambda = \lambda_i^*/\lambda^*$ where $\lambda^* = \lambda/(1 + e_0)$ was assumed.

*** A higher b value chosen in the active zone in order to consider the post-peak strain softening observed in CK₀UC tests.

index, λ , was evaluated from the slope of the specific volume-stress curve of the CRS tests. The ratio between the intrinsic and natural compression index, λ_i/λ , was assumed to be 0.3, based on the results of oedometer tests on reconstituted clay samples with similar properties [27,48].

Unloading reloading oedometer tests were not performed, and hence the swelling index, κ , was adjusted in order to obtain a good match of the triaxial tests stress-strain behavior.

The anisotropy parameters, initial inclination of the yield surface, α_0 , and soil constants that control the absolute rate of rotation of the yield surface and the relative effectiveness of volumetric and deviatoric strains in rotating the yield surface, β and μ , were determined following the procedure described by Wheeler et al. [42] and values suggested by Zentar et al. [49]. Lower and upper bounds for destructuration parameters a and b were estimated according to equations presented by Gras et al. [50].

Computational results illustrating the deviator stress – axial strain, $q - \varepsilon_a$, and excess pore pressure – axial strain, $\Delta u - \varepsilon_a$, together with

laboratory test results are presented in Fig. 7. The magnitude of the peak deviator stress obtained from CK₀UC and CK₀UE tests is very well captured with the model. The computed $q - \varepsilon_a$ relationship post-peak and also $\Delta u - \varepsilon_a$ of the CK₀UE tests from both 5 and 7 m depth agree well with results from CK₀UE tests. However, the rate of post-peak strain softening and Δu development observed from the CK₀UC tests cannot be accurately predicted from the computed results, probably due to formation and progression of shear bands and strain localization in the highly sensitive clay in the laboratory tests, where the failure mode was a distinct shear plane failure.

3.2.2. Lime-cement columns

The majority of previously published FE analyses involving cement improved clay have used either a total stress analysis based on Mohr-Coulomb failure criteria, based on results from UC tests, or a linear elastic model to describe the material properties of deep mixing columns [12,51–58].

In recent years several advanced constitutive material models for cemented clay, based on the critical state framework, have been presented [59–68]. A failure surface parallel to that of the untreated clay is usually adopted, considering the effect of initial cementation as well as cementation degradation through a modified mean effective stress, and by introducing model parameters and additional hardening rules to capture the hardening behavior up to peak stress and post-peak softening behavior. Although the main features of the behavior of cemented clays from compression laboratory data are captured reasonably well, an isotropic failure surface is assumed and the material strength is thereby independent of the stress path at loading. Also, a large number of model parameters are required, making it difficult to implement the models for calculation of complex geotechnical boundary value problems.

In this study the Hardening Soil model, HS, [19] implemented in PLAXIS was used to model the stress-strain behavior of the lime-cement columns. The HS model is an isotropic hardening double surface plasticity model that has proven to give realistic displacement results especially for excavation problems. The model combines Mohr-Coulomb failure criteria with a hyperbolic stress-strain relationship that allows for stiffness degradation. Similar to critical stress models, different stiffness moduli are adopted in HS for primary loading and unloading-reloading conditions.

The HS model allows an undrained effective stress analysis to be

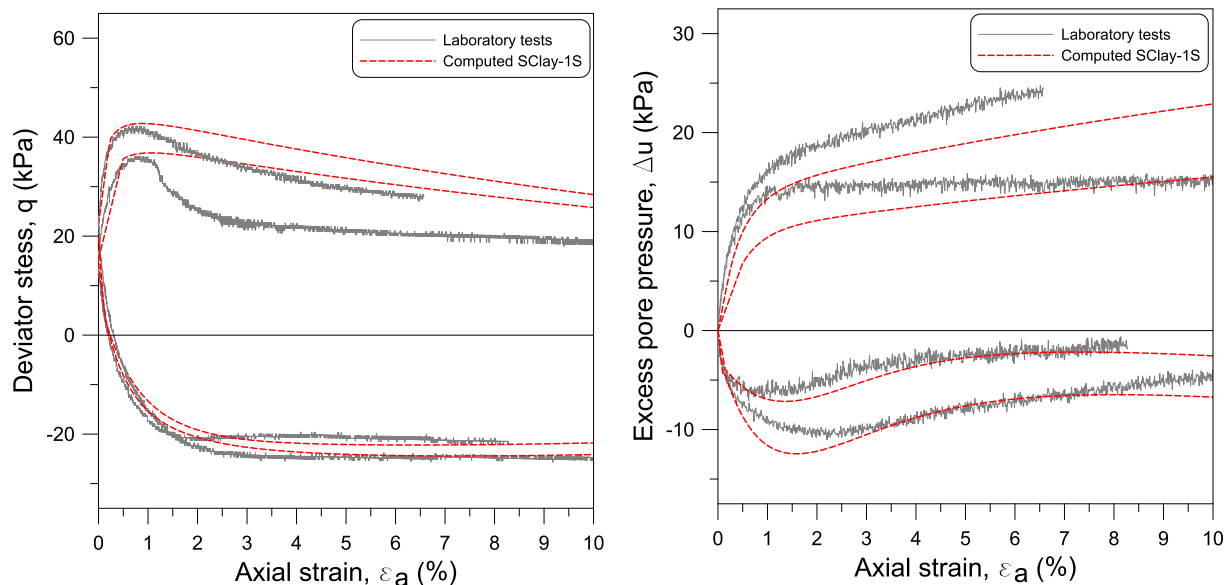


Fig. 7. Comparison of deviator stress/excess pore pressure - axial strain relationship between PLAXIS “Soil Test” with S-Clay1S material model and triaxial compression/extension tests on soft clay.

Table 4
Material parameters of lime-cement columns.

	Lime Cement Columns
Material model	Hardening Soil
Material behavior	Undrained B
Unit weight, γ (kN/m ³)	15.4* / 17.1*
Vertical pre-overburden pressure, POP (kPa)	224–192 **
Friction angle, ϕ	–
Undrained shear strength, $s_{u\text{col}}$ (kPa)	$0.5\sigma'_c(1.2\ln(OCR) + 0.95)$ ***
Secant stiffness, E_{50}^{ref} (kPa)	$1120s_{u\text{col}}$
Tangent stiffness, $E_{\text{oed}}^{\text{ref}}$ (kPa)	E_{50}^{ref}
Unloading/reloading stiffness, E_{ur}^{ref} (kPa)	$3E_{50}^{\text{ref}}$
Power of stress level dependency, m	0.7
Failure ratio, R_f	0.9
Poisson's ratio for unloading/reloading, ν_{ur}	0.2
Interface strength, R_{inter}	0.8

* Chosen equal to the unit weight of the clay layers.

** Varies with depth (σ'_{v0}).

*** σ'_c assumed equal to σ'_{v0} , varies with depth.

performed either with drained Mohr-Coulomb strength parameters, c and ϕ (Undrained A), or undrained strength parameters with $\phi = 0$ and $c = s_u$ (Undrained B). Commonly, the strength of lime-cement columns is assessed with unconfined compression tests. The lime-cement columns in the passive zone of the SPW, however, were subjected to a combination of unloading and lateral loading stress paths in the experimental test. Hence, CIUE_{UL} triaxial tests were considered to best represent the stress-strain behavior of the experimental LCC. A direct input of s_u based on CIUE_{UL} tests, [39], was adopted using $\phi'_{\text{col}} = 0$ and $c_{\text{col}} = s_{u\text{col}}$, where $s_{u\text{col}}$ increased with depth as:

$$s_{u\text{col}} = 0.5q_f = 0.5\sigma'_c(1.2\ln(OCR) + 0.95) \quad (1)$$

The HS model requires three stiffness parameters, E_{50}^{ref} , $E_{\text{oed}}^{\text{ref}}$ and E_{ur}^{ref} , that are stress dependent reference stiffness, and hence not model constants. However, once undrained strength parameters are specified the material loses its stress dependency of stiffness and the reference stiffness becomes equal to the actual stiffness. The reference secant modulus, E_{50}^{ref} , was chosen following the relationship obtained from CIUE_{UL} tests, $E_{50} = 560q_f$. The oedometer reference modulus for one-dimensional compression, $E_{\text{oed}}^{\text{ref}}$, that controls the magnitude of the plastic strain associated with the yield cap will be of minor importance on the passive side of the excavation and was chosen as $E_{\text{oed}}^{\text{ref}} = E_{50}^{\text{ref}}$. The

small strain stiffness modulus, E_0 , evaluated from resonant column tests performed on each sample, [39], varied between 147 and 245 MPa (mean 217 MPa). The unloading-reloading reference modulus E_{ur}^{ref} was chosen as $E_{ur}^{\text{ref}} = 3E_{50}$, that is approximately of the same magnitude as E_0 .

Comparison of the triaxial extension tests and PLAXIS “Soil test” for LCC, with material parameters according to Table 4, are presented in Fig. 8 as the deviator stress versus shear strain, $q - \epsilon_s$, and effective stress paths in $p' - q$ stress space, where p' is the mean effective stress. The overall stress – strain behavior, and also the effective stress paths obtained from the laboratory tests were reasonably captured by the HS model for all consolidation stresses.

3.2.3. Dry crust, Frictional soil, LDP and structural elements

Similar to LCC, the HS model was chosen to describe the strength and stiffness parameters of the dry crust and the frictional soil below the soft clay. No laboratory tests on the dry crust were conducted due to difficulties in obtaining undisturbed samples. Instead, the strength and stiffness material properties of the dry crust and the frictional soil were based on reported properties of similar soils with parameters according to Table 5.

The stiff LDP, constructed on site from compacted stony gravel, two layers of wooden beams and steel plates, was modeled as a linear elastic material. Linear elastic material properties, presented in Table 6, were chosen for the structural elements.

3.2.4. Interface properties

Interface elements were added on both sides of the plate elements representing the SPW in order to account for the soil-structure interaction. For the constitutive model S-Clay1S, implemented as a user defined model in Plaxis, the interface material properties are described by the MC strength parameters c' and ϕ and ψ . Values of $c' = 1$ and $\phi = 10^\circ$ and $\psi = 0$ were chosen in the analyses to consider the high sensitivity of the clay, and to account for the disturbance effect due to SPW installation. Sensitivity analyses on the effect of R_{inter} (by varying the value of ϕ by +50%) showed that the strength properties representing R_{inter} had no significant impact on the results. For the DM columns and for the dry crust the value of R_{inter} was chosen according to Table 4 and Table 5 respectively.

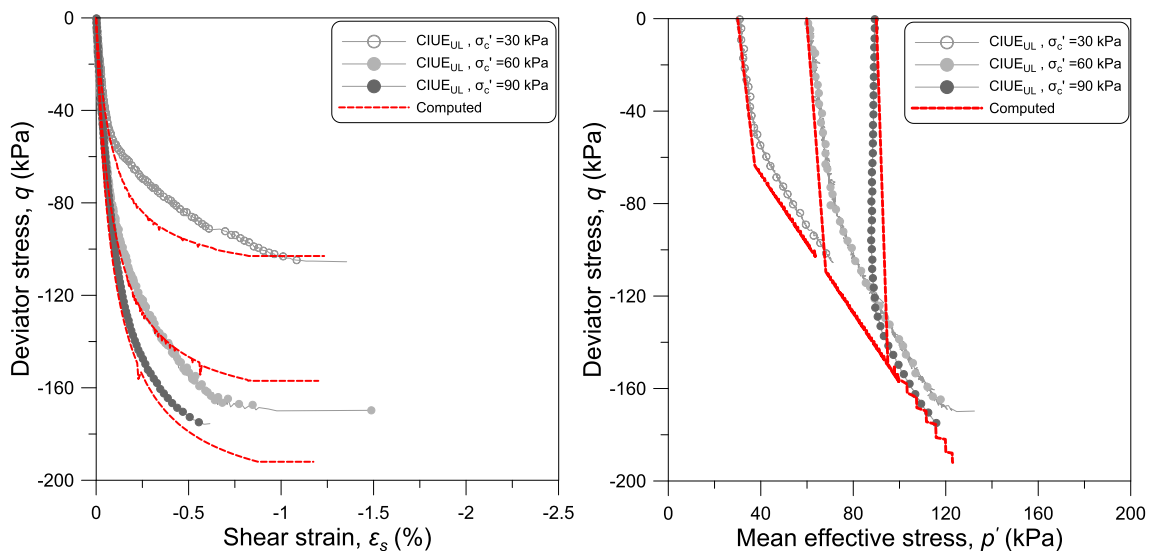


Fig. 8. Comparison of stress - strain relationship and effective stress paths between PLAXIS “Soil Test” and triaxial extension tests on lime-cement improved clay.

Table 5
Material properties used in FE analyses.

	Dry crust	Sand/Silt	LDP
Material model	Hardening Soil	Hardening Soil	Linear elastic
Material behavior	Undrained B	Drained	Non porous
Unit weight, γ/γ' (kN/m ³)	17.5/17.5	18/21	18/18
OCR	5	1	–
Friction angle, ϕ'	–	34	–
Dilatancy angle, ψ	–	4	–
Effective cohesion, c' (kPa)	–	0.1	–
Undrained shear strength, s_u (kPa)	30–15z*	–	–
Secant stiffness, E_{s0}^{ref} (kPa)	4000	25,000	–
Tangent stiffness, E_{oed}^{ref} (kPa)	4000	20,000	–
Unloading/Reloading stiffness, E_{ur}^{ref} (kPa)	12,000	75,000	–
Power of stress level dependency, m	1.0	0.5	–
Failure ratio, R_f	0.9	0.9	–
Poisson's ratio for unloading/reloading, ν_{ur}	0.2	0.2	–
Young's modulus, E , (kPa)	–	–	50,000
Poisson's ratio, ν	–	–	0.2
Interface strength, R_{inter}	0.5	–	–

* z refers to depth below the top of the layer, 0–1 m.

Table 6
Material properties of structural elements.

	SPW	Strut system
Element type	Plate, VL604	Beam, HEB300
Material behavior	Linear elastic	Linear elastic
Unit weight, γ (kN/m ³)	78.5	78.5
Height, h , (m)	0.36	–
Young's modulus, E , (kPa)	210×10^6	210×10^6
Axial stiffness, EA , (kN)	–	3.131×10^6
Flexural rigidity against bending around the principal axis, El_1 , (kN m ²), (vertical direction for SPW)	14.100×10^6	5.286×10^4
Flexural rigidity against bending around the secondary axis, El_2 , (kN m ²), (lateral direction for SPW)	2.820×10^5	1.798×10^4

4. Results and discussion

4.1. Failure load and effect of soil improvement on SPW stability

Calculated q_{peakFE} and q_{failFE} from the FE analyses are presented in Table 7 and compared with the experimental field test results, $q_{peakexp}$ and $q_{failexp}$. An overall good agreement between FE and experimental test results regarding q_{fail} was obtained for both Test A and Test B. The observed failure in Test A was initiated in the clay between the LCC panels due to the large LCC panel center distance of 3.0 m, immediately followed by failure of the columns closest to the SPW. The post-peak behavior of the clay thereby has a major influence on the magnitude of q_{failFE} in test A.

Both the observed $q_{failexp}$ and the failure mechanism of Test B, a failure simultaneously initiated in the clay and LCC panels, were well predicted by the FE analyses. For a center distance between the LCC panels of 1.5 m as in Test B, the properties of the LCCs have a larger impact on the failure mechanism compared to Test A, and a very good

agreement between q_{failFE} and $q_{failexp}$ was also obtained.

The calculated q_{peakFE} in Test B underestimated $q_{peakexp}$ by approximately 10%. The deviation between q_{peakFE} and $q_{peakexp}$ for Test B is probably due to the faster load rate applied in the last loading stage of Test B, which the rate-independent model in not able to capture. The load rate has a significant impact on $q_{peakexp}$ as a direct consequence of the rate dependency of s_u [69–72] and a lower loading rate would have likely resulted in a lower $q_{peakexp}$.

Comparative analyses, Test A2 and Test B2 in Table 7, were conducted using a bi-linear elastic perfectly plastic stress-strain material model with MC failure criteria and isotropic s_{ucol} evaluated as 50% of the UC strength ($q_{UCmean} = 192$ kPa) and $E_{col} = 165q_{UC}$ according to the relationship presented in Fig. 6. These analyses significantly overestimated $q_{failexp}$ in both tests, as seen in Table 7.

The ratio between the mobilized shear strength and the maximum shear stress, τ_{mob}/τ_{max} , shows the development of the failure mechanism in the column panels. At τ_{mob}/τ_{max} above 90%, see Figs. 9 and 10 (only every second column panel is presented for Test B for a clearer picture

Table 7
Comparison between measured and FE analyses-calculated failure load.

Field tests			FE-analyses				
Test	$q_{peakexp}$ (kPa)	$q_{failexp}$ (kPa)	Test	Type of analysis	q_{peakFE} (kPa)	q_{failFE} (kPa)	$\frac{q_{failFE}}{q_{failexp}}$
Test A	40.6	39.0	Test A1	Anisotropic strength	41.6	41.0	1.05
			Test A2	Isotropic strength	51.5	50.9	1.31
Test B	56.0	50.5	Test B1	Anisotropic strength	50.7	49.8	0.99
			Test B2	Isotropic strength	57.3	57.1	1.13

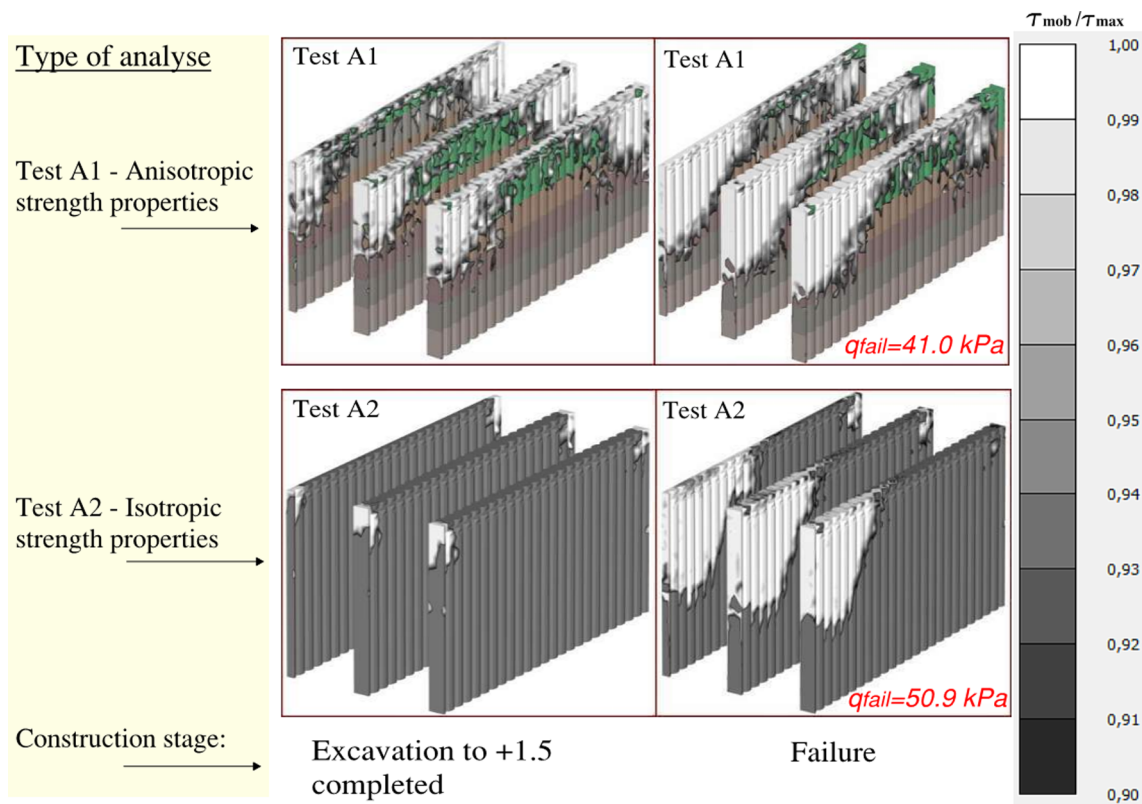


Fig. 9. Ratio between mobilized shear strength and maximum shear strength: Test A.

with the part of the column panels that is not covered by the scale on the right showing the material color instead) implies for a hyperbolic stress-strain relationship significant stiffness degradation causing large

plastic shear strains and significant yielding. In addition to the hyperbolic stress-strain relationship, consideration of strength anisotropy results in a significant difference in the development and propagation of

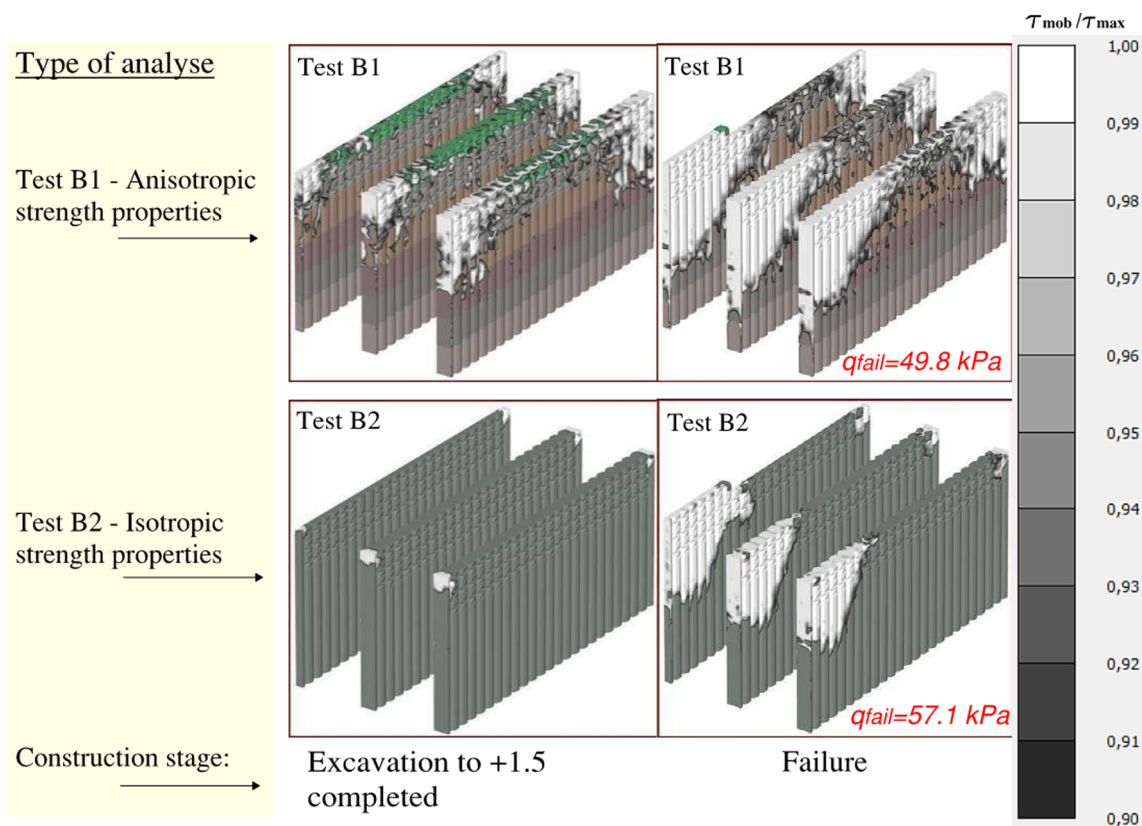


Fig. 10. Ratio between mobilized shear strength and maximum shear strength: Test B.

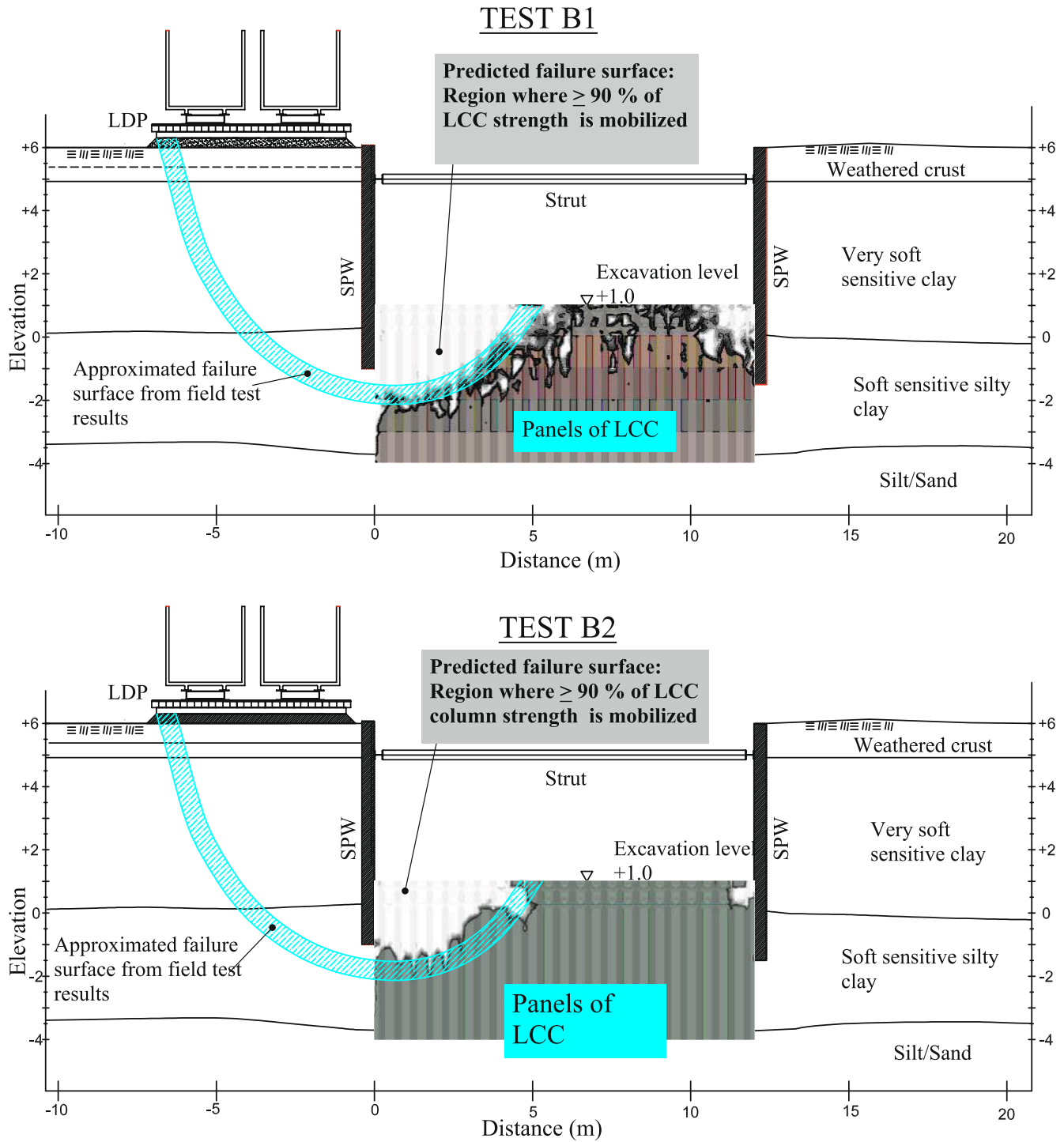


Fig. 11. Comparison between predicted and observed failure surface in the column panels: Test B.

the failure mechanism (Test A1 and Test B1) compared to the analyses performed with the isotropic strength properties and linear-perfectly plastic stress-strain relationship (Test A2 and Test B2). Also, the location of the failure surface in the LCC panels differed between the two types of analyses, as presented in Fig. 11 for Test B. The location of the failure surface from the experimental results was approximately interpreted to be located between the two measurement points with the largest observed difference in incremental u_h at failure. Due to higher $s_{u,col}$ in Test B2, a shallower failure surface compared to the experimental test was predicted, with a smaller part of the column panel (local failure) involved and starting in the passive zone just below the

toe of the SPW. On the other hand, in Test B1 the depth and extension of the predicted failure surface agrees significantly better with the experimental results than that predicted in Test B2. The more local failure of the LCC panels in Test B2 would explain the smaller ratio of q_{fail} between Test B, $q_{failB2}/q_{failB1} = 1.15$, and Test A, $q_{failA2}/q_{failA1} = 1.24$, predicted by the different analyses, although the area improvement ratio, A_{s3} , in Test B, $A_{sTestB} = 35\%$, was twice as large as in Test A, $A_{sTestA} = 17.5\%$.

The effect of soil improvement on the failure mechanism was investigated by excluding the LCCs in the numerical model, referred to as Case C (4.5 m excavation in unstabilized clay). Calculated q_{fail} for Case

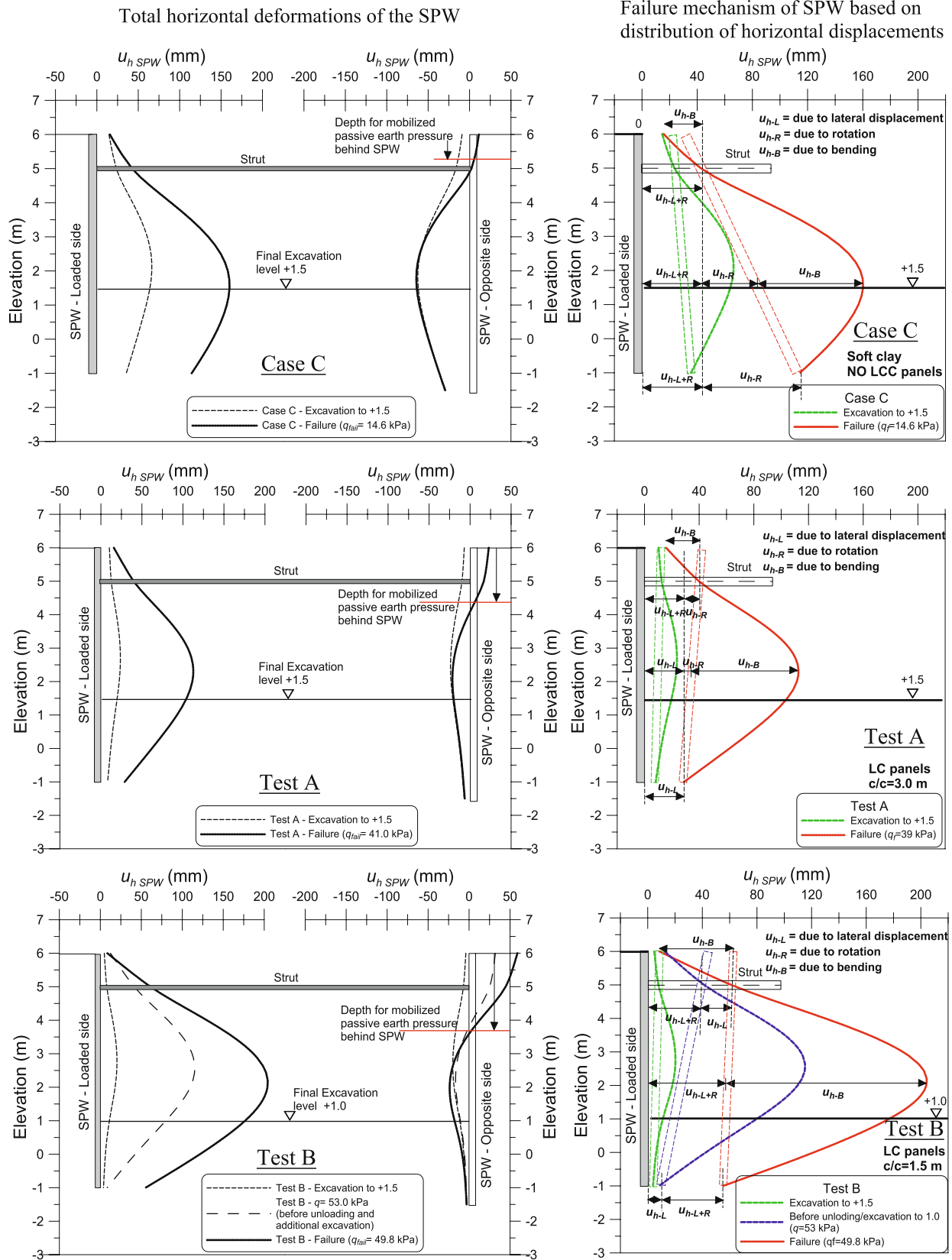


Fig. 12. Comparison of calculated horizontal displacements and failure mechanism of the sheet pile wall between Case C, Test A and Test B.

C was equal to 14.6 kPa after excavation to a depth of 4.5 m and a different failure mechanism of the SPW was predicted in the FE-analyses when LCC panels were not included in the model. Calculated total horizontal deformations of the loaded and the opposite SPWs, u_{hSPW} , at

a center location between the column panels (in Case C at the same location as Test A) are compared to Test A and Test B and presented in Fig. 12 (left side). The change in failure mechanism based on distribution of the horizontal displacements for each analysis is also

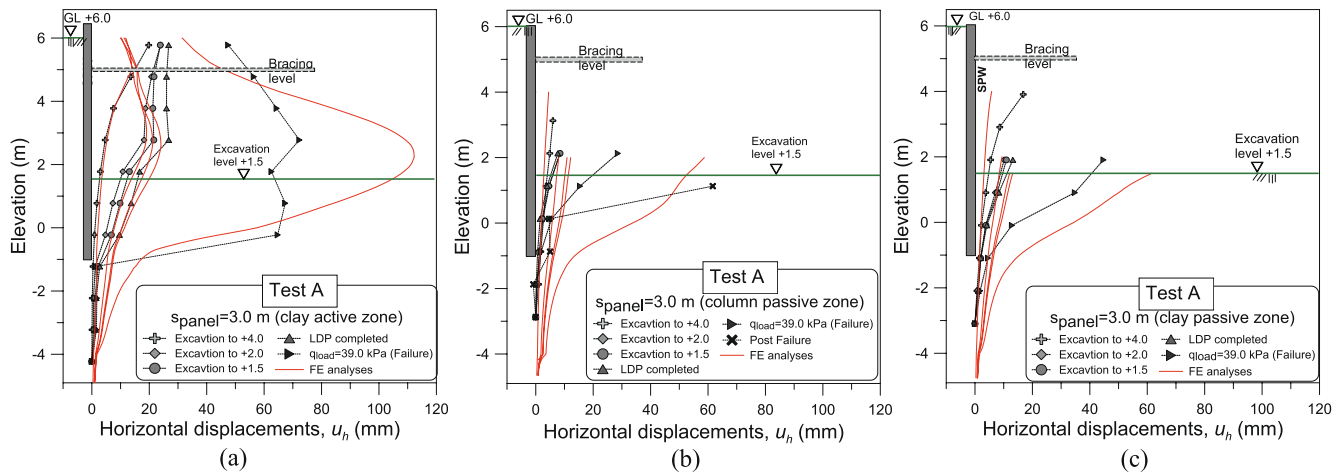


Fig. 13. Comparison of measured and calculated horizontal deformations for Test A; (a) active zone; (b) passive zone - LCC panels; (c) passive zone – clay between the LCC panels.

displayed in Fig. 12 (right side). Without LCC panels, large u_{hSPW} at the toe of the SPW on the loading side was predicted due to the low strength and stiffness properties of the clay. The rotation center of the loaded SPW is located at the bracing level due to the weak support below the bottom of the excavation, resulting in large rotational displacements at the toe of the SPW and low mobilization (evaluated as the depth where the direction of u_{hSPW} changes from negative to positive) of the soil behind the opposite SPW.

The LCC panels in Test A and Test B act as support for the SPW, reducing u_{hSPW} below the bottom of the excavation due to significantly higher strength and stiffness. In addition, due to the LCC panels below the excavation, the soil behind the opposite SPW is mobilized to a greater depth, due to the alteration in location of the rotational displacements of the SPWs. With increasing stiffness below the bottom of the excavation the rotation center is shifted downward in both Test A and Test B, as emphasized in Fig. 12. In Test A, $s_{panel} = 3.0$ m, a small inward rotation of the loaded SPW at the bracing level is predicted, suggesting that the support provided by the bracing system and the improved soil below the bottom of the excavation is of the same magnitude. On the other hand, in Test B, $s_{panel} = 1.5$ m, for the initial loading stage significantly larger inward rotation of the loaded SPW at the bracing level was indicated due to increased stiffness below the bottom of the excavation, resulting in a higher mobilization of the soil behind the opposite SPW. However, in the last loading stage after the additional excavation, the rotation center of the SPW was shifted and

increasing rotation induced displacements were indicated at the toe of the SPW. The change in rotation induced displacements from the bracing level to the toe of the SPW displayed in Test B is due to the significant yielding and stiffness degradation in the column panels in the last loading stage prior to failure, and the support below the bottom of the excavation was thus erased.

The failure mechanism will thereby have an impact on the magnitude of q_{fail} . The SPW improvement ratio is defined here as the ratio between q_{fail} for Test A and B calculated from the FE analyses and the calculated q_{fail} of case C. In the field tests failure of Test B occurred following a 5.0 m depth excavation, however, in order to compare q_{fail} at the same conditions, an additional FE analyses of Test B was performed for the 4.5 m deep excavation before the applied load was increased to failure. The SPW improvement ratio was about 2.8 and 4.1 for Test A and Test B respectively. Thereby, it can be emphasized that the SPW improvement ratio is not only related to the A_s but also to the type of failure mechanism.

4.1.1. Horizontal deformations

The predicted horizontal deformations, u_h , at the same locations as the inclinometers installed in the active and the passive zone of the SPWs are presented in Figs. 13 and 14 for different construction stages. For both Test A and Test B, predicted u_h agree well with those observed at small strain levels, during the excavation stages on both sides of the SPW. Predicted u_h at failure for Test A were overestimated in the clay,

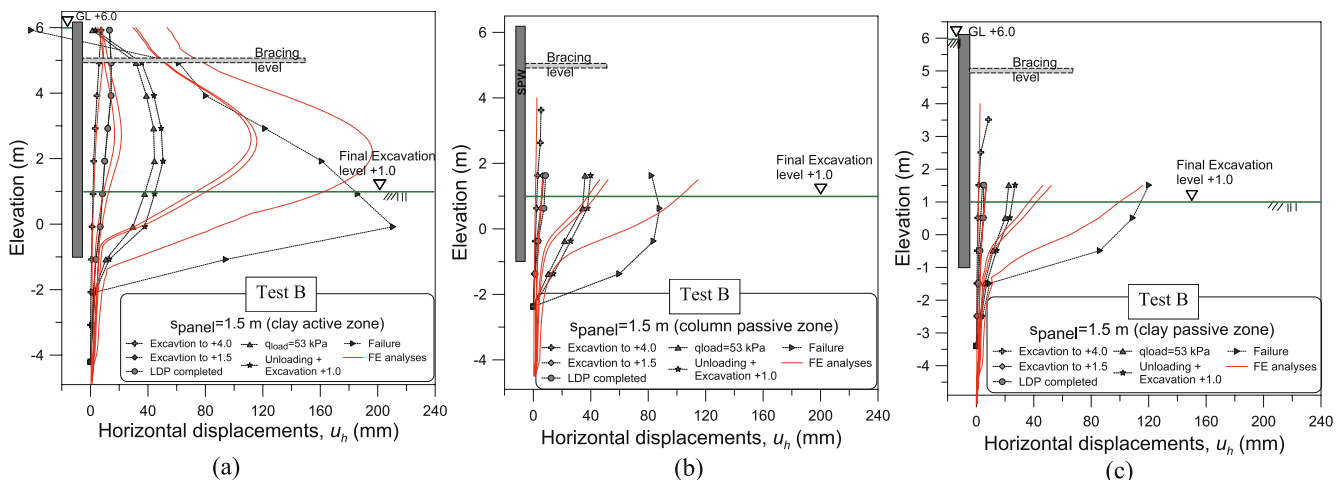


Fig. 14. Comparison of measured and calculated horizontal deformations for Test B; (a) active zone; (b) passive zone - LCC panels; (c) passive zone – clay between the LCC panels.

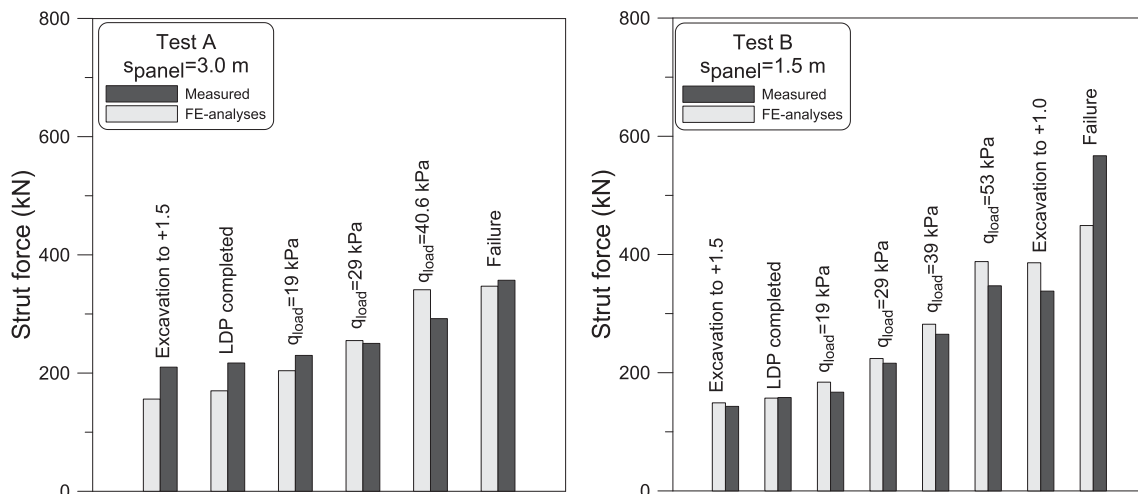


Fig. 15. Observed and calculated strut forces in Test A and Test B.

as well as in the column panel, even though the location of the predicted maximum u_h was correctly predicted. A reasonably good agreement was predicted at failure in Test B although the location of the calculated maximum u_h in the active zone differed slightly from that observed.

The interaction between the SPW, soft clay and very stiff LCC panels is very complex, making it very challenging to correctly predict the horizontal displacements at failure. The rate of post-peak strength reduction observed in the CK₀UC tests, Fig. 7, could not be completely reflected with the chosen set of destructuration parameters, and may have influenced predicted u_h . Also, increased loading behind the SPW resulted in increasing elastoplastic deformations predicted in the clay and LCC panels during the loading stages. However, only small incremental deformations was observed in the experimental tests during loading, followed by rapidly increasing creep deformations being observed prior to failure. Creep-induced displacements, which were not considered in the calculations, combined with potential underestimation of σ'_{vp} due to possible sample disturbance is also a possible reason for the deviation between calculated and measured u_h during the loading stages.

4.1.2. Strut forces

The observed and calculated strut forces after completed excavation and at different loading stages until failure are presented in Fig. 15. In general, a fairly good agreement between the predicted strut forces, F_{scale} and observed strut forces, F_{smeas} , was obtained with a maximum deviation between the ratio F_{scale}/F_{smeas} equal to 0.74 for Test A and 0.79 for Test B. In Test A, the ratio $F_{scale}/F_{smeas} = 0.74$ in the excavation stage, but increased for every loading stage and at failure a good agreement with $F_{scale}/F_{smeas} = 0.97$ was obtained. On the other hand, in Test B a good agreement was obtained after the excavation-, initial loading stages and final additional excavation with $F_{scale}/F_{smeas} = 0.99$ –1.14 but at failure F_{smeas} was underestimated and $F_{scale}/F_{smeas} = 0.79$.

The deviation between the observed and the measured F_s are most likely due to differences between the observed and the calculated post-peak stress-strain behavior of the column panels. In Test B, after the last load step was applied a significant decrease of $\Delta\sigma_{hol}$ was accompanied by a large increase of F_{smeas} , indicating load transfer from the column panels to the strut system. The chosen constitutive model, the HS model, does not consider post-peak strength degradation, resulting in underestimation of F_{smeas} at failure.

As already discussed, the undrained creep of the sensitive clay may have had some impact. The soil disturbance due to column installation and the heat generated by the column installation can significantly affect the creep properties of the sensitive clay, see [73]. To investigate

these effects further, future analyses should consider using a temperature-dependent creep model that also account for the anisotropy and destructuration as necessary for sensitive clays.

5. Conclusions

Lime-cement columns (LCCs) are increasingly used to support the bottom of deep excavations in soft clays. This paper presents numerical back-analyses analyses of failure tests of full-scale sheet-piled excavations in soft sensitive clay [18], where the bottom of the excavation is supported by panels of overlapping lime-cement columns (LCC). In order to understand and generalize these results, 3D finite element analyses were performed. The main challenge was how to model the sensitive soft soil and the LCCs on the passive side of the excavation. Namely, for the latter the conventional isotropic unconfined compression strength and stiffness may not be representative.

The soft clay was modelled with the rate-independent S-Clay1S model [20,21] that is able to represent the emerging anisotropic stiffness and strength of the sensitive clays, as well as the post-peak strain softening. The values for the model parameters were derived from anisotropically consolidated undrained triaxial compression and extension tests and constant rate of strain oedometer tests. The appropriateness of the model parameters was validated at element level, to confirm that the model is able to reproduce the soft clay response (see Fig. 7), before commencing to the analyses of the full-scale problems.

Given the stress-path in the LCC panels involves a combination of unloading and lateral loading, undrained extension tests were conducted on lime-cement admixed clay from the test site, considering different consolidation stresses and loading regimes. Isotropically consolidated compression tests and unconfined compression tests were also used as a reference. The model parameters for the Hardening Soil model in Plaxis, used to model LCCs, were calibrated against the isotropically consolidated undrained extension tests that involved combined unloading and lateral loading, as the most representative stress path (see Fig. 8). As a reference, numerical simulations of the full-scale excavations were also conducted without the columns (Case C) and using strength parameters evaluated from unconfined compression tests (Cases A2 and B2).

The FE analyses show that the predicted failure load with column strength parameters evaluated from the undrained triaxial extension tests was in good agreement with the observed failure load. On the other hand, analyses with column strength parameters evaluated from unconfined compression tests significantly over-predicted the observed failure in both Test A and Test B. Therefore, it is strongly recommended that in projects where LCCs are used on passive side, consolidated

undrained extension tests are performed, or alternatively a constitutive model that is able to represent the emerging materials response under arbitrary stress paths is used.

Overall, the FE simulations are in good agreement with the field test results, and demonstrate how the column panels installed in the passive zone act as support below the bottom of the excavation. Increasing the area improvement ratio (i.e. decreasing the c/c distance between LCC panels), changes the failure mechanism by altering the location of the center of rotation of the SPW (see Fig. 12). A reasonably good agreement between the predicted and the measured horizontal displacements was obtained for the excavation stages of both tests (Figs. 13 and 14). The predicted strut forces at failure in Test A were in very good agreement with observed values (Fig. 15). However, most likely because the constitutive model could not accurately capture the post-peak stress-strain behavior of the column panels, the strut forces at failure in Test B were underestimated.

Rate-effects were not considered, given the low hydraulic conductivity of the clay and the short duration of the field test. However, undrained creep of the sensitive clay may have influenced the response in the field. Modelling those effects, however, is not trivial: the soil disturbance due to column installation and the heat generated by the curing of the columns can significantly affect the creep properties of the sensitive clay (see [73]). To investigate these effects further, future analyses should consider using a suitable temperature-dependent creep model. Further work is also needed to be able to simulate the response of LCCs under arbitrary stress paths, so that the model parameter could be derived based on standard tests.

Declaration of Competing Interest

The authors declare that they have no known competing financial interests or personal relationships that could have appeared to influence the work reported in this paper.

Acknowledgments

This study is part of the BIG (Better Interaction in Geotechnics) project. The authors wish to acknowledge the support provided by Skanska Sweden AB, the Development Fund of the Swedish Construction Industry, and the Swedish Transport Administration. We would also like to thank the anonymous referees, as their constructive comments truly helped us to improve the manuscript.

References

- [1] Tanaka H. Behaviour of braced excavations stabilized by deep mixing method. *Soils Found* 1993;33(2):105–15.
- [2] O'Rourke TD, O'Donnell CJ. Field behavior of excavation stabilized by deep soil mixing. *J Geotech Geoenviron Eng* 1997;123(6):516–24.
- [3] O'Rourke TD, McGinn AJ. Case history of deep mixing soil stabilization for boston central artery. *Geotech Special Publ (GSP)*, ASCE 2004;126(1):77–136. [https://doi.org/10.1061/40744\(154\)3](https://doi.org/10.1061/40744(154)3).
- [4] O'Rourke TD, McGinn AJ. Lessons learned for ground movements and soil stabilization from the Boston central artery. *J Geotech Geoenviron Eng* 2006;131:966–89.
- [5] Hsieh HS, Wang CC, Ou CY. Use of jet grouting to limit diaphragm wall displacement of a deep excavation. *J Geotech Geoenviron Eng* 2003;129(2):146–57.
- [6] Hsi JP, Yu JBY. Jet grout application for excavation in soft marine clay. *Proc Int Conf Soil Mech Geotech Eng* 2005;16(3):1485.
- [7] Khan MRA, Hayano K, Kitazume M. Investigation on stability of sheet pile quay wall improved by cement treated sea-side ground from centrifuge model tests. *Soils Found* 2008;48(4):563–75.
- [8] Ou Chang-Yu, Teng Fu-Chen, Wang I-Wen. Analysis and design of partial ground improvement in deep excavations. *Comput Geotech* 2008;35(4):576–84. <https://doi.org/10.1016/j.compgeo.2007.09.005>.
- [9] Ou CY, Hsieh PG, Lin YL. A parametric study of wall deflections in deep excavations with the installation of cross walls. *Comput Geotech* 2013;50:55–65.
- [10] Ruggeri P, Frizzetti VME, Vita A, Segato D, Scarpelli G. Stiffness of wall-type grouting under transversal loading. *Ground Improvement* 2014;167:4:301–10.
- [11] Liao HJ, Su SF. Base stability of grout pile-reinforced excavations in soft clay. *J Geotech Geoenviron Eng* 2011;138(2):184–92.
- [12] Ignat Razvan, Baker Sadek, Larsson Stefan, Liedberg Sven. Two- and three-dimensional analyses of excavation support with rows of dry deep mixing columns. *Comput Geotech* 2015;66:16–30. <https://doi.org/10.1016/j.compgeo.2015.01.011>.
- [13] Su SF, Liao HJ. Base stability of deep excavation in clay reinforced with grout piles. *Engineers-Ground Improvement*; 2017.
- [14] Ou CY, Wu TS, Hsieh HS. Analysis of deep excavation with column type of ground improvement in soft clay. *J Geotech Eng* 1996;122(9):709–16.
- [15] Su SF. Anisotropic strength evaluation of clay reinforced with grout piles. *J Geotech Geoenviron Eng* 2009;135(10):1529–37.
- [16] Yang T, Tan TS, Leung CF. Mass behaviour of embedded improved soil raft in an excavation. *Proc Inst Civ Engrs – Geotech Eng* 2011;164(GE1):11–25.
- [17] Sukponya Atijit, Jotisankasa Apinit. Large simple shear testing of soft Bangkok clay stabilized with soil-cement-columns and its application. *Soils Found* 2016;56(4):640–51. <https://doi.org/10.1016/j.sandf.2016.07.005>.
- [18] Ignat R, Baker S, Liedberg S, Larsson S. Behaviour of braced excavation supported by panels of deep mixing columns. *Can Geotech J* 2016;53(10):1671–87.
- [19] Schanz T, Vermeer PA, Bonnier PG. The hardening soil model: formulation and verification. *Beyond 2000 in computational geotechnics*, 1999. p. 281–96.
- [20] Koskinen M, Karstunen M, Wheeler SJ. Modelling destructuration and anisotropy of a soft natural clay. *Proceedings of 5th European Conf. Numerical Methods in Geotechnical Engineering*, P. Mestat, ed., Presses de l'ENPC/LCPC, Paris, France, 2002. p. 11–20.
- [21] Karstunen M, Krenn H, Wheeler SJ, Koskinen M, Zentar R. Effect of anisotropy and destructuration on the behavior of Murro test embankment. *Int J Geomech* 2005;5(2):87–97.
- [22] Sivasithamparan N. Development and implementation of advanced soft soil models in finite elements PhD-thesis University of Strathclyde; 2012.
- [23] Bjerrum L. Problems of soil mechanics and construction on soft clays and structurally unstable soils. In *Proc. 8th ICSMFE*; Vol. 3, 1973, p. 111–59.
- [24] Larsson R. Basic behaviour of Scandinavian soft clays. Linköping: Swedish Geotechnical Institute; 1977. p. 129 p.
- [25] Länsvaara T. A study of the mechanical behavior of soft clay. Norway: Dissertation, Norwegian University of Science and Technology; 1999.
- [26] Karlsrud K, Hernandez-Martinez FG. Strength and deformation properties of Norwegian clays from laboratory tests on high-quality block samples. *Can Geotech J* 2013;50(12):1273–93.
- [27] Koskinen M. Plastic anisotropy and destructuration of soft Finnish clays PhD thesis Aalto University, Helsinki; 2014.
- [28] D'Ignazio M. Undrained shear strength of Finnish clays for stability analyses of embankments Ph D. thesis Tampere: Tampere University of Technology; 2016.
- [29] Ignat R. Field and laboratory tests of laterally loaded rows of lime-cement columns Licentiate thesis KTH Royal Institute of Technology; 2015.
- [30] Thakur V. Strain localization in sensitive soft clays PhD thesis Trondheim: NTNU; 2007.
- [31] Gylland AS, Jostad HP, Nordal S. Experimental study of strain localization in sensitive clays. *Acta Geotech* 2014;9(2):227–40.
- [32] Larsson R, Sällfors G, Bengtsson PE, Alén C, Bergdahl U, Eriksson L. Shear strength-Evaluation in cohesion soils. Information 3. Linköping: Swedish Geotechnical Institute (SGI); 2007. (in Swedish).
- [33] Ladd C, Foott R. New design procedure for stability of soft clays. *ASCE J Geotech Eng Div* 1974;100(GT7):763–86.
- [34] Jamiolkowski M, Ladd CC, Germaine JT, Lancelotta R. New developments in field and laboratory testing of soils. *Proc 11th Int Conf on Soil Mechanics and Foundation Engineering*, San Francisco 1985;Vol. 1:57–153.
- [35] Mayne PW. Stress anisotropy effects on clay strength. *ASCE J Geotech Eng* 1985;111:356–66.
- [36] Ladd CC. Stability evaluation during staged construction. *ASCE J Geotech Eng* 1991;117(4):540–615.
- [37] Tanaka H, Locat J, Shibuya S, Soon TT, Shiwakoti DR. Characterization of Singapore, Bangkok, and Ariake clays. *Can Geotech J* 2001;38(2):378–400.
- [38] Won JY. Anisotropic strength ratio and plasticity index of natural clays. In *Proceedings of the 18th International Conference on Soil Mechanics and Geotechnical Engineering*. 2013. p. 2–6.
- [39] Ignat R, Baker S, Holmén M, Larsson S. Triaxial extension and tension tests on lime-cement-improved clay. *Soils Found* 2019. <https://doi.org/10.1016/j.sandf.2019.06.004>.
- [40] Åhnberg H. Consolidation stress effects on the strength of stabilized Swedish soils. *Ground Improvement* 2006;10(1):1–13.
- [41] Kasama Kiyonobu, Zen Kouki, Iwataki Kiyoharu. Undrained shear strength of cement-treated soils. *S&F* 2006;46(2):221–32. <https://doi.org/10.3208/sandf.46.221>.
- [42] Wheeler SJ, Näättäen A, Karstunen M, Lojander M. An anisotropic elastoplastic model for soft clays. *Can Geotech J* 2003;40(2):403–18.
- [43] Gens A, Nova R. Conceptual bases for a constitutive model for bonded soils and weak rocks. In: Anagnostopoulos et al., editors. *Geotechnical Engineering of Hard Soils-Soft Rocks*, Athens, Greece. Balkema: Rotterdam; 1993. p. 485–94.
- [44] Koskinen M, Lojander M, Tolla P, Vepsäläinen P. Numerical analysis on Murro test embankment. In: Mestat P, editor. *Proceedings of 5th European Conf. Numerical Methods in Geotechnical Engineering*, Presses de l'ENPC/LCPC, Paris, France, 2002b. p. 397–402.
- [45] Karstunen M, Koskinen M. Plastic anisotropy of soft reconstituted clays. *Can Geotech J* 2008;45(3):314–28.
- [46] Karstunen M, Koskinen M. Anisotropy and destructuration of Murro clay. *Jardine RJ, Potts DM, Higgins KG, editors. Advances in geotechnical engineering: The Skempton Memorial conference*, on 29–31 March 2004, Vol. 1. London, UK: Thomas Telford Publishing; 2004. p. 476–87.
- [47] Yildiz A, Karstunen M, Krenn H. Effect of anisotropy and destructuration on behavior of Haarajoki test embankment. *Int J Geomech* 2009;9(4):153–68.
- [48] Wood T. On the small strain stiffness of some Scandinavian clays and impact on

- deep excavation PhD thesis Chalmers University of Technology; 2016.
- [49] Zentar R, Karstunen M, Wheeler SJ. Influence of anisotropy and destructuration on undrained shearing of natural clays. In: Proceedings of 5th European Conf. Numerical Methods in Geotechnical Engineering, P. Mestat, ed., Presses de l'ENPC/LCPC, Paris, France, 2002. p. 21–26.
- [50] Gras JP, Sivasithamparam N, Karstunen M, Dijkstra J. Permissible range of model parameters for natural fine-grained materials. *Acta Geotechnica* 2018;13(2):387–98.
- [51] Navin MP. Stability of embankments founded on soft soil improved with deep-mixing-method columns PhD dissertation Blacksburg VA: Virginia Polytechnic Institute and State University; 2005.
- [52] Adams TE. Stability of levees and floodwalls supported by deep-mixed shear walls: five case studies in the New Orleans area. Virginia Polytechnic Institute and State University, Blacksburg VA; 2011.
- [53] Jamsawang P, Voottipruex P, Boathong P, Mairaing W, Horpibulsuk S. Three-dimensional numerical investigation on lateral movement and factor of safety of slopes stabilized with deep cement mixing column rows. *Eng Geol* 2015;188:159–67.
- [54] Jamsawang P, Voottipruex P, Jongpradist P, Bergado DT. Parameters affecting the lateral movements of compound deep cement mixing walls by numerical simulations and parametric analyses. *Acta Geotechnica* 2015;10(6):797–812.
- [55] Jamsawang P, Boathong P, Mairaing W, Jongpradist P. Undrained creep failure of a drainage canal slope stabilized with deep cement mixing columns. *Landslides* 2016;13(5):939–55.
- [56] Jamsawang P, Yoobanpot N, Thanasisathit N, Voottipruex P, Jongpradist P. Three-dimensional numerical analysis of a DCM column-supported highway embankment. *Comput Geotech* 2016;72:42–56.
- [57] Jamsawang P, Jamnam S, Jongpradist P, Tanseng P, Horpibulsuk S. Numerical analysis of lateral movements and strut forces in deep cement mixing walls with top-down construction in soft clay. *Comput Geotech* 2017;88:174–81.
- [58] Chai JC, Shrestha S, Hino T, Uchikoshi T. Predicting bending failure of CDM columns under embankment loading. *Comput Geotech* 2017;91:169–78.
- [59] Kasama Kiyonobu, Ochiai Hidetoshi, Yasufuku Noriyuki. On the stress-strain behaviour of lightly cemented clay based on an extended critical state concept. *Soils Found* 2000;40(5):37–47. <https://doi.org/10.3208/sandf.40.5.37>.
- [60] Liu MD, Carter JP. A structured Cam Clay model. *Can Geotech J* 2002;39(6):1313–32.
- [61] Suebsuk Jirayut, Horpibulsuk Suksun, Liu Martin D. Modified structured cam clay: A generalised critical state model for destructured, naturally structured and artificially structured clays. *Comput Geotech* 2010;37(7-8):956–68. <https://doi.org/10.1016/j.compgeo.2010.08.002>.
- [62] Suebsuk Jirayut, Horpibulsuk Suksun, Liu Martin D. A critical state model for overconsolidated structured clays. *Comput Geotech* 2011;38(5):648–58. <https://doi.org/10.1016/j.compgeo.2011.03.010>.
- [63] Horpibulsuk S, Liu MD, Liyanapathirana DS, Suebsuk J. Behaviour of cemented clay simulated via the theoretical framework of the Structured Cam Clay model. *Comput Geotech* 2010;37(1-2):1–9.
- [64] Horpibulsuk S, Liu MD. Structured cam clay model with cementation effect. *Geotech Eng J SEAGS AGSSEA* 2015;46(1):86–94.
- [65] Arroyo M, Ciantia M, Castellanza R, Gens A, Nova R. Simulation of cement-improved clay structures with a bonded elasto-plastic model: A practical approach. *Comput Geotech* 2012;45:140–50.
- [66] Nguyen LD, Fatahi B, Khabbaz H. A constitutive model for cemented clays capturing cementation degradation. *Int J Plast* 2014;56:1–18.
- [67] Robin V, Javadi AA, Cuisinier O, Masroufi F. An effective constitutive model for lime treated soils. *Comput Geotech* 2015;66:189–202.
- [68] Xiao H, Lee F, Liu Y. Bounding surface cam-clay model with cohesion for cement-admixed clay. *Int J Geomech* 2017;17(1):1–22.
- [69] Graham J, Crooks JH, Bell AL. Time effects on the stress-strain behaviour of natural soft clays. *Géotechnique* 1983;33(3):327–40.
- [70] Leroueil S, Kabbaj M, Tavenas F, Bouchard R. Stress-strain-strain rate relation for the compressibility of sensitive natural clays. *Géotechnique* 1985;35(2):159–80.
- [71] Lefebvre G, LeBoeuf D. Rate effects and cyclic loading of sensitive clays. *J Geotech Eng* 1987;113(5):476–89.
- [72] Sheahan TC, Ladd CC, Germaine JT. Rate-dependent undrained shear behavior of saturated clay. *J Geotech Eng* 1996;122(2):99–108.
- [73] Li Y, Dijkstra J, Karstunen M. Thermomechanical creep in sensitive clays. *J Geotech Geoenviron Eng* 2018;144(11):04018085.